International Journal of Heat and Mass Transfer 182 (2022) 121929

Contents lists available at ScienceDirect

International Journal of Heat and Mass Transfer

journal homepage: www.elsevier.com/locate/hmt

Linear stability analysis of horizontal convection under a Gay-Lussac type approximation

Peyman Mayeli*, Tzekih Tsai, Gregory J. Sheard

Department of Mechanical and Aerospace Engineering, Monash University, VIC 3800, Australia.

ARTICLE INFO

Article history:
Received 4 July 2021
Revised 20 August 2021
Accepted 1 September 2021

Keywords:
Gay-Lussac approximation
Non-Boussinesq approximation
Horizontal convection
Linear stability analysis

ABSTRACT

A linear stability analysis is conducted for horizontal natural convection under a Gay-Lussac (GL) type approximation in a relatively shallow enclosure cavity. The GL type approximation is developed based on extending density variations to the advection term as well as gravity term through the momentum equation. Such a treatment invokes the GL parameter ($Ga = \beta\Delta\theta$) as the non-Boussinesq parameter with a physical value ranging $0 \leq Ga \leq 2$, characterising deviation from the classic Boussinesq approximation. Results are compared against the Boussinesq approximation in terms of the Nusselt number and skin friction. Extreme values of Ga are found to produce a counter-rotating convection cell at the hot end of the enclosure at higher Rayleigh numbers - a feature absent from Boussinesq natural convection modeling. For stability analysis purposes, linearized perturbation equations under the GL type approximation are derived and solved to characterise the breakdown of the steady two-dimensional solution to infinitesimal three-dimensional disturbances. Stability results predict that the flow remains stable up to $Ra_{cr1} = 6.46 \times 10^8$ for the Boussinesq case ($Ga = 0$), and then with increasing Ga the flow briefly stabilises to $Ga \cong 0.2$, then becomes progressively more unstable with futher increases in Ga, yielding a critical Rayleigh number $Ra_{cr2} = 4.23 \times 10^8$ at $Ga_{max} = 2$. Three-dimensional transition is predicted to be via an oscillatory instability mode of the steady base flow having a spanwise wavelength that increases as Rayleigh number increases. 3D-DNS simulations verify the linear stability analysis predictions in terms of growth rate, and elucidate the mode shapes achieved at saturation.

1. Introduction

Horizontal convection (HC) is a distinct class of NC in which the fluid is heated unevenly across a horizontal boundary. Due to HC contribution in scientific applications such as earth's oceanic [1-3] and atmospheric [4-6] flow patterns and the insight that it provides for the industrial processes such as glass melting [7-8], this class of NC has attracted the attention of researchers during the recent decade. As an idealised representation of myriad natural convection systems, numerical simulation of HC is often performed within enclosed domains, such as square and rectangular wall-heated enclosures with buoyancy supplied either from the upper or lower horizontal boundary. For instance, oceanic circulation constitutes transportation of warm fluids from the tropical regions to high latitudes, where it cools and sinks, subsequently before an up-welling flow across the ocean basin completes the flow path [9].

Recent decades have seen a resurgence of horizontal convection research. Chiu-Webster et al. [8], studied the HC for very viscous fluids in rectangular cavities with aspect ratios ranging $0.01 \leq A \leq 2$ up to $Ra = 10^{10}$ and reported Rossby's [10] famous one-fifth power scaling of the average Nusselt number ($Nu_{ave} \sim Ra^{1/5}$) for HC. A similar study was performed by Sheard & King [11] for several aspect ratios ranging $0.16 \leq A \leq 2$ up to $Ra = 10^{10}$ at $Pr = 6.14$. They reported aspect ratio dependence of Nu_{ave} and boundary layer thickness at low Ra, whereas these become independent of aspect ratio for higher Ra once convection becomes the most dominant part of the heat transfer mechanism. Hossain et al. [12] analysed HC for very small aspect ratios ranging $0.001 \leq A \leq 0.16$ relevant to oceanic scale at $Pr = 6.14$ up to $Ra = 10^{12}$. They found that the transition from the diffusion-dominated regime to convection-dominated regime scales with A^{-4}, whereas the corresponding average Nusselt number at the threshold was proportional to A itself. Tsai et al. [13] studied linear stability analysis of HC in a rather shallow rectangular cavity with an aspect ratio of 0.16 under the OB approximation. Their computations indicate that the flow field remains stable up to $Ra = 3.2 \times 10^8$ for the Prandtl number spanning $0.1 \leq Pr \leq 10$. Tsai et al. [14] also conducted stability analysis of HC with different temperature profiles for the heating

* Corresponding author.
E-mail addresses: peyman.mayeli@monash.edu (P. Mayeli), Tzekih.Tsai@monash.edu (T. Tsai), Greg.Sheard@monash.edu (G.J. Sheard).

https://doi.org/10.1016/j.ijheatmasstransfer.2021.121929
0017-9310/

Nomenclature

A	Height to length aspect ratio
c_f	skin friction coefficient
e_g	unit vector in gravity direction
Fr	Froude number
g	gravity
Ga	Gay-Lussac parameter ($\beta\Delta\theta$)
H	height of the cavity
k	spanwise wavenumber
L	length of the cavity
N_f	Number of Fourier modes
Nu	Nusselt number
p	pressure
p^*	modified pressure
P	dimensionless pressure
Pr	Prandtl number
Ra	Rayleigh number
T	Temperature
x	coordinate vector
X	dimensionless coordinate vector
u	velocity vector
U	dimensionless velocity vector
$\hat{U}$	eigenmode
α	thermal diffusivity
β	isobaric expansion coefficient
θ	physical temperature
Θ	dimensionless temperature
μ	kinematic viscosity
μ	eigenvalue
ν	kinematic viscosity
ρ	density
ρ_0	reference density
τ_w	wall shear stress
ϕ	gravitational potential

Subscript

ave	average
c	cool
h	hot
loc	local
tot	total
ref	reference

part of the geometry. They found that transition from steady to time-periodic convection occurs through a supercritical bifurcation across all imposed temperature profiles, with the step profile being the most unstable one. Linear stability analysis of HC under the OB approximation is also performed by Passaggia et al. [15] for a step temperature distribution along the horizontal surface in a cavity with A = 0.25 at Pr = 1. They considered Dirichlet and free-slip boundary conditions for their simulations and reported the critical Rayleigh number equal to 2×10^7 and 1.7×10^8, respectively. Lyubimov et al. [16] studied the Rayleigh-Bénard-Marangoni system with horizontal temperature gradient under a weakly compressible type approach in which the momentum and continuity equations were considered compressible while the energy equation is treated as incompressible.

In all of these aforementioned works, HC was analysed under the Oberbeck–Boussinesq (OB) approximation, which is restricted by different assumptions such as small temperature differences. A review of different scenarios for non-OB simulation of natural convection related problems can be found in Ref. 17. One of the incompressible-based strategies to go beyond the OB approximation is the Gay-Lussac (GL) approach, which is developed based on considering density variations beyond the buoyancy term of the momentum equations, i.e. continuity and the advection/convection terms of the momentum and energy equations, respectively. An emergent feature of this approach is the GL parameter comprising the product of the volumetric thermal expansion coefficient (β) and the reference temperature difference ($\Delta\theta$). Pesso & Piva [18] used this strategy for the square cavity benchmark problem with large density variations. Recently, a GL-type approach was proposed by Lopez et al. [19] for non-OB treatment of rapidly rotating flows, in which density variations were extended only to the centrifugal part of the advection term to capture centrifugal effects arising from background rotation in those rapidly rotating flows. Mayeli & Sheard [20-21] continued this approach and showed that the GL parameter may be also expressed in terms of the Rayleigh, Prandtl, and Froude numbers (Ga = RaPrFr) with a maximum value ($Ga_{max} = 2$) to avoid an unphysical density value.

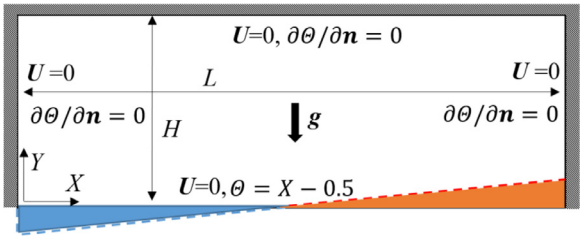

Fig. 1. A schematic of the HC problem and boundary conditions in a rectangular enclosure.

The aim of this study is to investigate the effects of the GL modification to buoyancy on the dynamics, heat transfer and linear stability of horizontal convection flow. The rest of the paper is organized as follows. In section 2, geometry and boundary conditions are described. In section 3, the non-OB approximation is demonstrated, and linearized perturbation equations under the GL type approximation are presented. Section 4 deals with the temperature difference, local Nusselt number and friction coefficient results obtained from the GL and OB approximations. Stability analysis results are presented and compared against the DNS results in Section 5. Finally, conclusions are drawn in Section 6.

2. Horizontal convection problem and boundary conditions

The GL-type approximation is applied for the HC problem in a rectangular enclosure with a fixed aspect ratio A = H/L = 0.16. A schematic of the problem associated with boundary conditions is shown in Fig. 1. In this problem, a linear temperature distribution is applied along the bottom wall while other surfaces are thermally isolated (zero temperature gradient normal to the walls), and the fluid is taken to have a constant Prandtl number Pr = 1, applicable to fluids including air. Therefore, the fluid is cooled and heated up along the left and right side of the bottom wall, respectively, and a counter-clockwise circulation is formed due to a buoyancy-driven flow. A no-slip boundary condition is imposed on all boundaries for the velocity.

3. Governing equations under the Gay-Lussac approximation and numerical consideartions

The GL approximation is an incompressible based strategy that follows the fundamentals of the OB approximation including negligible viscous heat dissipation, constant thermophysical properties, small temperature differences, and small hydrostatic pressure variations compared to thermodynamic presseure variations. However

under the GL approximation for buoyancy-driven flows, in contrast to the OB approximation in which the density variations are restricted to the gravity term, density variations are extended beyond the gravity term. Derivation of the governing equations under the GL approach begins with dividing the incompressible Navier–Stokes equations plus an advection-diffusion transport equation for temperature, taking density ρ to be variable, and dividing the equations by a reference density (ρ_0) in the absence of additional body forces and neglecting viscous heat dissipation in the energy equation,

$$\nabla \cdot \mathrm{u} = 0 \tag{1}$$

$$(\rho/\rho_0)\partial \mathrm{u}/\partial \mathrm{t}^* + (\rho/\rho_0)(\mathrm{u}\cdot\nabla)\mathrm{u} = -(1/\rho_0)\nabla \mathrm{p} + \nu\nabla^2\mathrm{u} + (\rho/\rho_0)\mathrm{e_g} \tag{2}$$

$$(\rho/\rho_0)\partial \mathrm{T}/\partial \mathrm{t}^* + (\rho/\rho_0)(\mathrm{u}\cdot\nabla)\mathrm{T} = \alpha\nabla^2\mathrm{T}. \tag{3}$$

Consistent with conventional application of the OB approximation, a linear state relation $\rho/\rho_0 = 1-\beta\theta$ connecting density to temperature is adopted. The dimensionless form of the governing mass conservation, momentum and temperature transport equations under the GL approximation may be written as

$$\nabla \cdot \mathrm{U} = 0 \tag{4}$$

$$(1-\mathrm{Ga}\Theta)\partial \mathrm{U}/\partial \mathrm{t} + (1-\mathrm{Ga}\Theta)(\mathrm{U}\cdot\nabla)\mathrm{U} = -\nabla \mathrm{P} + \mathrm{Pr}\,\nabla^2\mathrm{U} - \mathrm{RaPr}\Theta\mathrm{e_g} \tag{5}$$

$$(1-\mathrm{Ga}\Theta)\partial\Theta/\partial \mathrm{t} + (1-\mathrm{Ga}\Theta)(\mathrm{U}\cdot\nabla)\Theta = \nabla^2\Theta. \tag{6}$$

Here dimensionless symbols include velocity U, time t, pressure P and temperature Θ. These have respectively been non-dimensionalised by

$$\mathrm{t} = \frac{\mathrm{t}^*\alpha}{\mathrm{L}^2}, \mathrm{X} = \frac{\mathrm{x}}{\mathrm{L}},\ \mathrm{Y} = \frac{\mathrm{y}}{\mathrm{L}},\ \mathrm{U} = \frac{\mathrm{uL}}{\alpha}, \mathrm{P} = \frac{\mathrm{p}^*\mathrm{L}^2}{\rho\alpha^2},\ \Theta = \frac{\theta}{\Delta\theta} = \frac{\mathrm{T}-\mathrm{T}_0}{\mathrm{T}_h-\mathrm{T}_c}. \tag{7}$$

Eqs. (4-6) introduce the Gay-Lussac parameter $\mathrm{Ga} = \beta\Delta\theta$ that is twice of the relative temperature difference ($\mathrm{Ga} = 2\varepsilon$), a Rayleigh number characterising the ratio of buoyancy to viscous dissipation, $\mathrm{Ra} = \mathrm{g}\beta\Delta\theta\mathrm{L_{ref}}^3/\nu\alpha$, and the Prandtl number characterising the ratio of viscous to thermal dissipation, $\mathrm{Pr} = \nu/\alpha$. The Gay-Lussac paramter is equivalent to the Boussinesq parameter describing the relative density difference [22]. As it will be shown later, under this approach the Gay-Lussac paramter should not exceed a specified range for a physical density value. It should be noted that, since in the considered range of Ra and Ga at a fixed $\mathrm{Pr} = 1$, the base flow remains steady, non-Boussinesq effects are not considered in the transient terms. Also, $\mathrm{e_g}$ is the unit vector in the direction of gravity ($\mathrm{e_g} = \mathrm{g}/|\mathrm{g}|$).

It may be seen that as $\mathrm{Ga}\to 0$ ($\Delta\theta\to 0$), the governing equations under the conventional Boussinesq approximation are recovered. In the present formulation, $(1-\mathrm{Ga}\Theta)$ acts as a pre-factor on different terms and its effect becomes more important by increasing the reference temperature difference. In practice, Ga cannot exceed a specified value to avoid an unphysical (negative) density,

$$\rho/\rho_0 = 1-\beta\theta = 1-\beta\Delta\theta\Theta = 1-\mathrm{Ga}\Theta > 0. \tag{8}$$

Based on the defined dimensionless temperature, here the maximum Ga cannot exceed 2 ($\mathrm{Ga_{max}} = 2$). As mentioned earlier, Ga is a product of Rayleigh, Prandtl, and Froude numbers ($\mathrm{Ga} = \mathrm{RaPrFr}$), where Fr is the Froude number ($\mathrm{Fr} = \alpha^2/\mathrm{gL}^3$) characterising the ratio of inertia to gravity. It can be shown that, ignoring $(1-\mathrm{Ga}\Theta)$ prefactor from the continuity equation simplifies the the full GL approach as an incompressible based strategy and reduces the computational cost while the final results under two approaches are almost identical [23-24]. The simplified GL approach follows the same fundamentals of the Boussinesq approximation as mentioned earlier and physical range of the Gay-Lussac paramter. In this study, we follow the idea proposed by Lopez et al. [19], where a GL-type approximation was applied to the momentum advection term to capture centrifugal effects in rotating flows. Ignoring density variations in the momentum time derivative and thermal convection terms simplifies the GL approximation [20-21] to,

$$\nabla \cdot \mathrm{U} = 0 \tag{9}$$

$$\partial \mathrm{U}/\partial \mathrm{t} + (\mathrm{U}\cdot\nabla)\mathrm{U} = -\nabla \mathrm{P} + \mathrm{Pr}\,\nabla^2\mathrm{U} - \mathrm{RaPr}\Theta(\,\mathrm{e_g} - \mathrm{Fr}(\mathrm{U}\cdot\nabla)\mathrm{U}) \tag{10}$$

$$\partial\Theta/\partial \mathrm{t} + (\mathrm{U}\cdot\nabla)\Theta = \nabla^2\Theta. \tag{11}$$

Eq. (10) is consistent with the momentum equation under the OB approximation, except for the additional inertial buoyancy term on the right-hand side of the momentum equation. When expressed in this form, it is apparent that the action of this additional term is to modify the effective direction (and strength) of the gravity locally throughout the flow, which is ignored in the conventional Boussinesq approximation. Indeed, regions that are experiencing higher spatial accelerations described by $(\mathrm{U}\cdot\nabla)\mathrm{U}$, will experience deviations from the OB buoyancy approximation. The strength of these deviations relative to gravity is described by Fr, with $\mathrm{Fr}\to 0$ (hence $\mathrm{Ga}\to 0$) recovering the classical OB approximation.

The linearised Navier–Stokes equations under the GL-type approximation are derived in the conventional fashion, whereby velocity, pressure and temperature are decomposed into a 2D base flow and infinitesimal fluctuating disturbance component, i.e. $U = U_{2D} + U'$, $P = P_{2D} + P'$ and $\Theta = \Theta_{2D} + \Theta'$, where constant $|\varepsilon| << 1$. These decompositions are substituted into Eqs. (9) to (11), and retention of terms of order $O(\varepsilon)$ reveals the following equations,

$$\nabla \cdot \mathrm{U}' = 0, \tag{12}$$

$$\begin{aligned}\partial \mathrm{U}'/\partial \mathrm{t} &= \left[1-\mathrm{RaPrFr}\bar{\Theta}\right]\left((\bar{\mathrm{U}}\cdot\nabla)\mathrm{U}' + (\mathrm{U}'\cdot\nabla)\bar{\mathrm{U}}\right)\\ &= -\nabla \mathrm{P}' + \mathrm{Pr}\,\nabla^2\mathrm{U}' - \mathrm{RaPr}\Theta'\left(\mathrm{e_g} - \mathrm{Fr}\left(\bar{\mathrm{U}}\cdot\nabla\right)\bar{\mathrm{U}}\right),\end{aligned} \tag{13}$$

$$\partial\Theta'/\partial \mathrm{t} = -\left[\left(\bar{\mathrm{U}}\cdot\nabla\right)\Theta' + \left(\mathrm{U}'\cdot\nabla\right)\bar{\Theta}\right] + \nabla^2\Theta'. \tag{14}$$

A further important additional simplification is possible thanks to the invariance of the geometry in the spanwise direction. The flow variables may be represented as Fourier series in the z-direction, and a consequence of the linearization of Eqs. (12–14) is that each Fourier mode couples only with the 2D base flow, not other modes. It is therefore efficient to evolve individual 2D Fourier modes using the same spatial discretisation as used for the base flow, rather than evolving a full three-dimensional perturbation field. The dimensionless spanwise-periodic wavelength of an individual perturbation field, $\lambda = 2\pi/\mathrm{k}$, where k is the spanwise wavenumber characterising the perturbation. This reduces an evolution of a three-dimensional perturbation field to a set of 2D evolutions, with k emerging as an additional parameter to Rayleigh number, Froude number and Prandtl number. By defining $\mathrm{A}(\tau)$ to represent the linear evolution operator for time integration of a perturbation field comprising a single phase-locked spanwise Fourier mode $\hat{\mathrm{Q}} = (\hat{\mathrm{U}}, \hat{\mathrm{V}}, \hat{\mathrm{W}}, \hat{\Theta})^{\mathrm{T}}$ over time interval τ, i.e.

$$\hat{\mathrm{Q}}(\mathrm{t}+\tau) = \mathrm{A}(\tau)\hat{\mathrm{Q}}, \tag{15}$$

an eigenvalue problem may then be constructed as

$$\mathrm{A}(\tau)\hat{\mathrm{Q}}_\mathrm{k} = \mu_\mathrm{k}\hat{\mathrm{Q}}_\mathrm{k}, \tag{16}$$

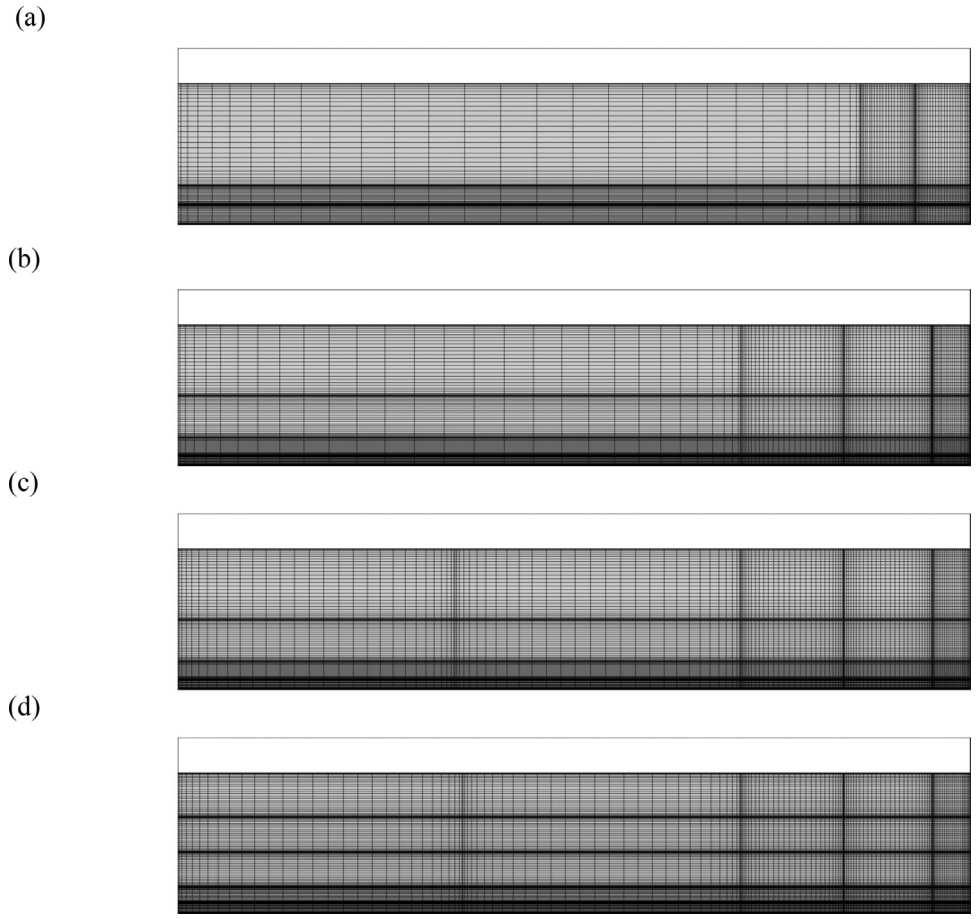

Fig. 2. Meshes having (a) 9 (b) 16 (c) 20 and (d) 25 elements, with intra-element grids displayed over the 30 × 30 quadrature points.

having complex eigenvalues μ_k and eigenvectors $\hat{Q}_k$. The eigenvalues μ_k relate to the exponential growth rate σ and angular frequency ω through $\mu = \exp[(\sigma + i\omega)\tau]$. Stability is determined by the magnitude of the leading eigenvalue, with $|\mu| = 1$ corresponding to neutral stability, while $|\mu| > 1$ and $|\mu| < 1$ respectively represent unstable and stable scenarios. As the base flows are time-invariant in this study, the analysis may proceed with an arbitrarily selected time interval τ. Stability analysis is performed by determining the leading eigenmode magnitude across a broad domain of wavenumbers ($0 \leq k \leq 70$). The bifurcation may be either synchronous ($\omega = 0$) or oscillatory ($\omega \neq 0$). Combinations of Ra and Ga are sought corresponding to neutral stability, i.e. $\sigma_{max} = 0$.

The eigenmodes for the stability analysis are computed using an implicitly restarted Arnoldi method [25-26] implemented through the ARPACK eigenvalue solver [27]. The present solver has been implemented and validated previously in [11-14].

The governing equations are spatially discretised using a high-order nodal spectral-element method and evolved in time using a third-order backward differentiation scheme [28]. The present code has been validated and employed in several natural convection problems [11-14]. To explore the mesh independence of the solutions, several meshes were constructed having different numbers of elements. In each mesh, elements were concentrated in the region where spatial flow variations are expected to be greatest: towards the heated end of the bottom boundary where buoyancy enters the flow. In each case, element polynomials of order $P = 30$ were adopted. The mesh independency is checked in terms of L_2 norm (taken here as the domain integral of the velocity magnitude) in Table 1 at $Ra = 4 \times 10^8$ and $Ga = 2$, with the meshes used being shown in Fig. 2. These parameters were chosen as they are expected to represent a taxing case to resolve. The computed L_2 norms obtained once the flows settled to their equilibrium states (see Table 1) indicate that the 20-element mesh resolves the flow to a high accuracy, and this resolution is used hereafter.

Table 1
Mesh resolution study of HC problem at $Ra = 4 \times 10^8$ and $Ga = 2$ with the different number of elements and a high order of Lagrangian polynomial (P=30).

Number of elements	L_2norm	$\lvert Difference\rvert(\%)$
9	21557.9175562921	2.096
16	21557.9627504395	6×10^{-5}
20	21557.9774402941	2×10^{-7}
25	21557.9775014154	–

A similar test was performed for the mesh having 20 elements and different orders of polynomials from $P = 20$ to 40 and it was found that, a polynomial of order $P = 30$ is sufficient for the mesh independency purposes.

Once the thermo-flow field is obtained, results are compared in terms of the local Nusselt number and skin friction. Since the flow the is thermally isolated from three sides in this study, local Nusselt number along the bottom horizontal wall is calculated as follow

$$Nu_{loc} = \left| \frac{\partial \Theta}{\partial Y} |_{wall} \right|. \quad (17)$$

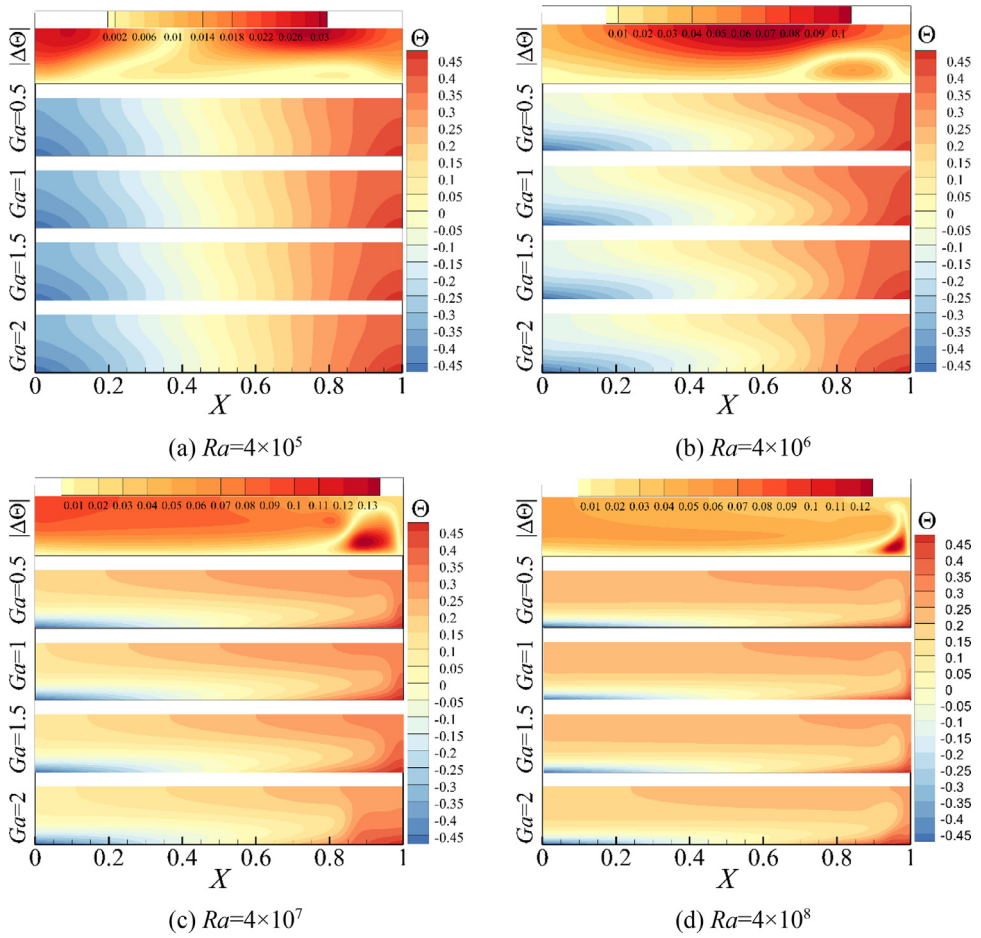

Fig. 3. Comparison of temperature fields at different Ra and Ga values, as stated. The top frame of each plot shows the absolute temperature difference between the Ga = 2 and Ga = 0 cases.

The friction coefficient along the surface based on the dimensionless velocity is defined as

$$c_f = -2\,\mathrm{Pr}\begin{bmatrix}\tau_{xx} & \tau_{xy}\\ \tau_{yx} & \tau_{yy}\end{bmatrix}\begin{bmatrix}n_x\\ n_y\end{bmatrix} = -2\mathrm{Pr}\begin{bmatrix}2\partial U/\partial X & \partial U/\partial Y+\partial V/\partial X\\ \partial U/\partial Y+\partial V/\partial X & 2\partial V/\partial Y\end{bmatrix}\begin{bmatrix}n_x\\ n_y\end{bmatrix}. \quad (18)$$

In Eq. (18), n_x and n_y are the normal vector of the surface in horizontal and vertical directions, respectively. The magnitude of friction coefficient is calculated as

$$c_f = \sqrt{(c_{fx})^2 + (c_{fy})^2} \quad (19)$$

4. Analysing thermo-flow field at different Gay-Lussac parameter values

Results of HC under the GL-type and OB approximations are analysed in this section. A qualitative comparison is performed by depicting the dimensionless temperature fields at different Ra and Ga starting from Ga_{max} at the bottom frame of each plot in Fig. 3. By decreasing Ga, the temperature field is evolved so that results under the OB approximation (Ga = 0) are retrieved. The top frame in each figure shows the absolute temperature difference between the GL-type approximation with $Ga_{max} = 2$ and results under the OB approximation (Ga = 0). At $Ra = 4 \times 10^5$ (Fig. 3a) conduction is still the dominant heat transfer mechanism, and temperature fields corresponding to different Ga values do not show a significant mismatch. In this state, the absolute temperature difference is observed mostly occurring along the top surface with a maximum value around 0.03 ($\Delta\Theta_{max} = 0.03$). As the Rayleigh number increases, the magnitude of the absolute temperature difference is also augmented in the top frame. Results start to show the centrifugal effects in Fig. 3b at $Ra = 4 \times 10^6$, where convection starts to become the dominant heat transfer mechanism and the effect of different Ga values is sensible across the bottom-right corner of the cavity. A comparison among temperature fields in Fig. 3b reveals that, under the GL-type approximation, by decreasing Ga value, isotherm-lines show less deformation in the horizontal direction, and most of the difference occurs in the vertical direction. Most of the temperature difference at this Rayleigh number still occurs along the top side with a maximum value of around 0.1 ($\Delta\Theta_{max} \cong 0.1$). At $Ra = 4 \times 10^7$ (Fig. 3c) where the flow is convection dominated, a thin thermal boundary layer is formed along the bottom side, and the effect of different Ga values is apparent on the temperature field, especially at the rising plume region across the bottom-right corner. Results indicate increasing Ga (and consequently the reference temperature difference) has a damping effect on the formation of the rising plume in convection-dominated regime. In other words, lower values of Ga let a broader area to be affected by the warming section of the bottom surface. At this Rayleigh number, large values of the temperature differences shift their location toward the bottom-right corner; however, apparent temperature differences along the top side are observable. Results at $Ra = 4 \times 10^8$ are presented in Fig. 3d. A significant difference among the temperature fields corresponding to the different Ga values is evident in this plot. Results

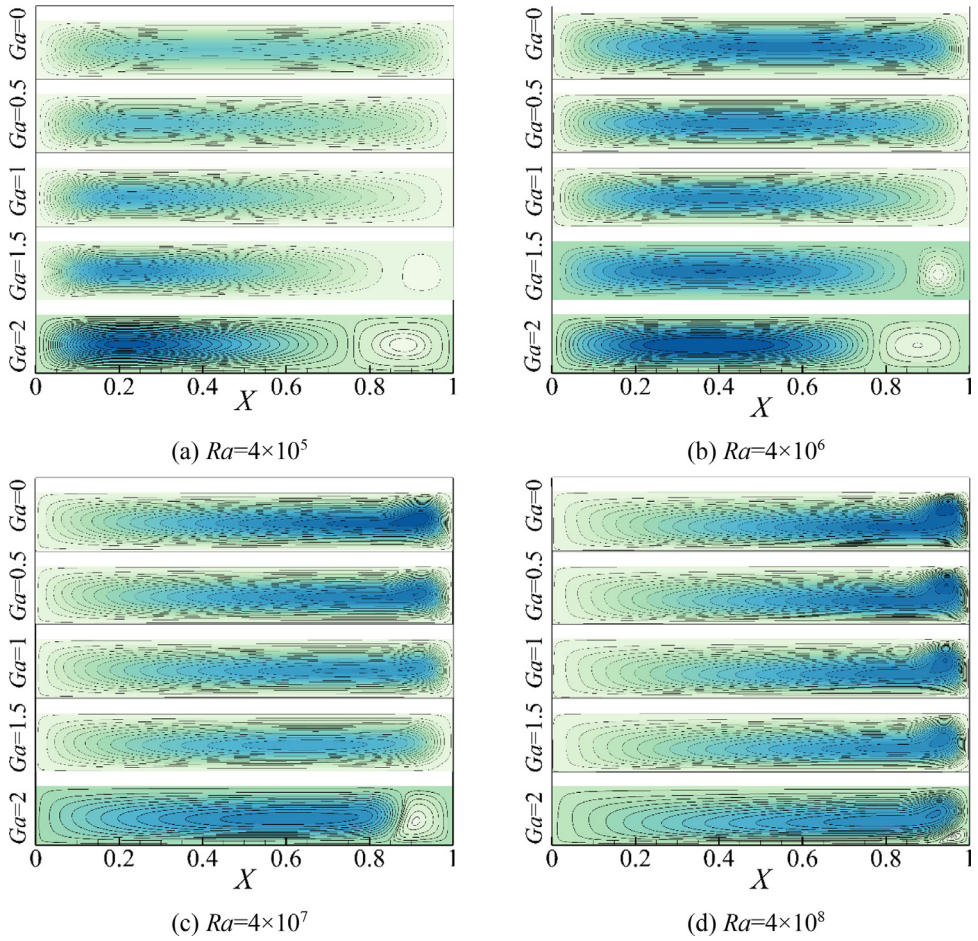

Fig. 4. A comparison of stream-function at different Ra and Ga values, as stated. The top frame of each plot shows the absolute temperature difference between Ga = 2 and Ga = 0. Dark to light shaded contours show respective maximum and minimum values of stream-function. The minimum and maximum of each figure's legend are set equal together.

indicate that, under the GL-type approximation, a thicker thermal boundary layer is formed along the horizontal bottom wall compared to the OB approximation. The damping effects of the larger Ga on the rising plume region are also visible in this figure. The maximum absolute difference at this high Rayleigh number is about 0.12, which concerning the maximum dimensionless temperature shows about 24% mismatch between Ga_{max} and Ga = 0 ($|\Delta\Theta|/\Theta_{max} = 0.24$).

In Fig. 4, stream-functions at different Ga and Ra are presented. In condution-dominated regime (Fig. 4a and b), two separate regions are distinguishable at the right half of the cavity for large GL parameters (Ga = 2 and 1.5) that are turned to smaller regions in the convection dominated regime (Fig. 4c and d). As seen, for small and moderate Ga (Ga = 0, 0.5, 1), up to $Ra = 4 \times 10^6$ there is an asymmetric distribution of the stream-function inside the geometry but by increasing the Rayleigh number, a stronger circulation forms across the top-right region of the enclosure, reflecting the plume effect to generate a strong circulation across this region.

4.1. Local Nusselt number

The local Nusselt number results at different Ra and Ga along the bottom wall are presented in Fig. 5. In general, the local Nusselt number is increased by increasing the Rayleigh number, as expected. At $Ra = 4 \times 10^5$ (Fig. 5a), the local Nusselt number has an almost symmetric distribution along both cooling and heating sections of the bottom wall, and it does not show sensitivity to Ga alteration. This behavior is attributed to a conduction-dominated regime at this Rayleigh number. As the Rayleigh is increased to $Ra = 4 \times 10^6$ (Fig. 5b), a clear mismatch among Nu_{loc} corresponding to different Ga values is visible. In this figure, the local Nusselt number undulates along the bottom wall so that its value for the higher Ga has a larger value only over of $0.3 \leq X \leq 0.65$.

In the convection-dominated regime (Fig. 5c and d), the local Nusselt number exhibits a linearly decreasing trend over the left part of the base, while over the right part, a linearly increasing trend is seen up to a maximum, before a significant deficit is produced. The linear regions are consistent with the formation of a convective boundary layer adjacent to the bottom surface. The significant reduction in the value of the local maximum in Nu_{loc} and the leftward shift in its horizontal location with increasing Ga underpins the local impact of centrifugal effects in the buoyancy supply region at the right side of the enclosure. This is underscored by this region containing the largest absolute differences in temperature between Ga = 0 and 2 cases, as shown earlier in Fig. 3(c,d). In this region, the horizontally convecting flow gains buoyancy and erupts vertically into the side-wall plume. This is a region comprising both rotation and thermal gradients inciting centrifugal effects.

4.2. Skin shear stress

The shear stress values across the horizontal boundaries are investigated in Fig. 6 in this section. The solid and dashed-lines show

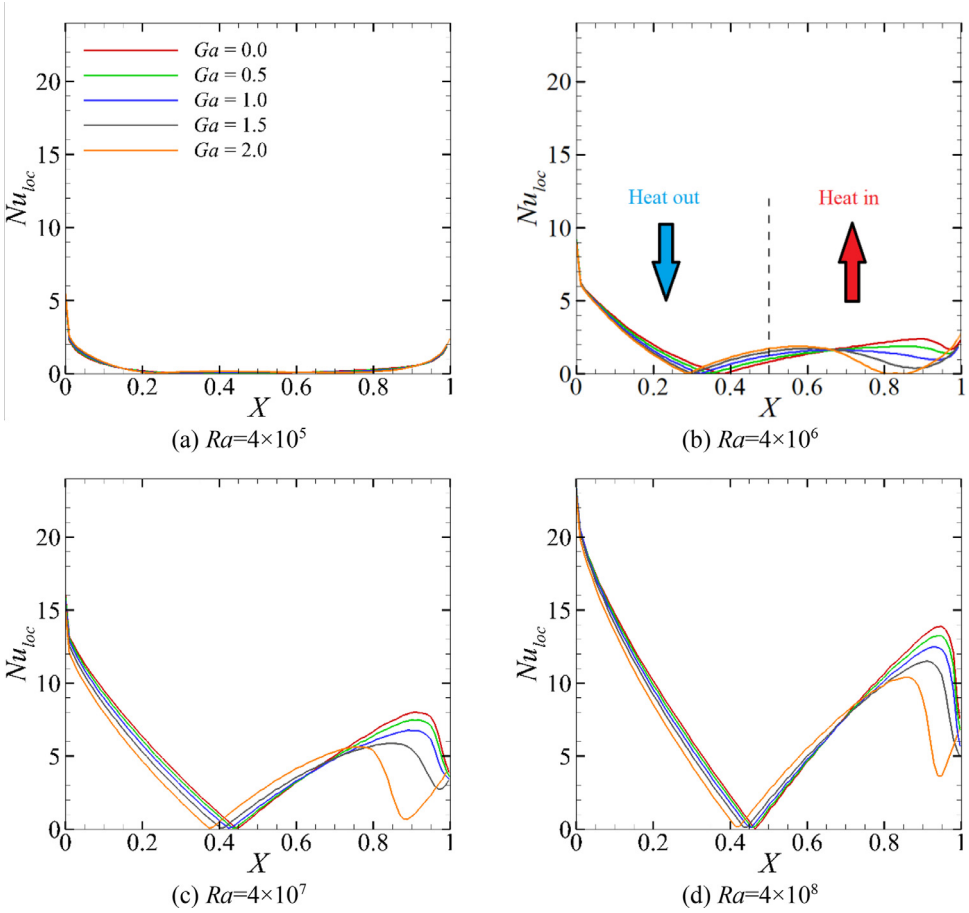

Fig. 5. The local Nusselt number distribution along the bottom surface at different Ra and Ga values as stated. Fig. 5b shows the cooling and heating sections along the bottom side.

the magnitude of the friction coefficient Eq. (19) along the bottom and top walls, respectively. In general, c_f is increased by increasing the Rayleigh number, as expected.

Results of the conduction dominated regime at $Ra = 4 \times 10^5$ (Fig. 6a) indicates c_f has a symmetric distribution along both surfaces at $Ga = 0$, but as the Ga is increased, a linear distribution is obtained for the c_f with a more considerable value along the bottom surface and a local maximum approximately at $X \cong 0.175$ for both surfaces at moderate Ga values ($Ga = 0.5$ & 1). A second local maximum is observed approximately at $X \cong 0.9$ for large Ga values ($Ga = 1.5$ & 2). Local maxima of the c_f along both horizontal surfaces at $Ga = 1.5$ and 2 may be attributed to the second core which is formed at high reference temperature differences (two bottom frames of Fig. 4a). A similar trend is observable for c_f distribution at $Ra = 4 \times 10^6$ in Fig. 6b. At $Ra = 4 \times 10^7$ (Figs. 6c) and $Ra = 4 \times 10^8$ (Fig. 6d), the general behavior of c_f distribution becomes reverse for the bottom wall so that a more symmetric distribution of the c_f is obtained by increasing Ga value. Another exciting feature of the c_f distribution at the convection-dominated regime is the large magnitude of this parameter along the top wall approximately at $X \cong 0.9$, which decreases by increasing Ga value. In other words, both of the Fig. 6c and d indicate that at convection dominated regime, the strong rising plume creates a large c_f value across the top-right region. Finally, the strange behavior of the c_f distribution at the bottom-right corner is attributed to the emergence of a counter-rotating cell (two bottom frames of Fig. 4c and d) at a high Ga value that is observable at convection-dominated regime. This feature is absent from simulations employing the conventional Boussinesq model ($Ga = 0$).

5. Stability analysis

Attention is now turned to the stability of these flows to small three-dimensional disturbances, and the effects of varying Rayleigh number, spanwise wavenumber and GL parameter at a fixed Prandtl number, $Pr = 1$. The precision of the eigenvalue μ and eigenmode $\hat{U}$ produced by subspace iteration is defined by the residual

$$R = \left\| A\hat{U} - \mu\hat{U} \right\| \tag{20}$$

where $\|\cdot\|$ is the vector norm. Obtaining the leading eigenvalue and the corresponding eigenmode at each wavenumber relies on an iterative process which is ceased as soon as $Res < 10^{-7}$ is achieved. Nevertheless, the eigenmodes are resolution-dependent. A mesh resolution study for the eigenvalue computations across wave number $0 \le k \le 70$ with different number of elements provided in Fig. 2 with a high polynomial degree of 30 within each element ($N_p = 30$) is performed. The absolute difference of the leading eigenvalues obtained from different mesh resolutions having 16, 20, and 25 elements are checked at $Ra = 4 \times 10^8$ with $Ga = 2$ and $Ra = 6.5 \times 10^8$ with $Ga = 0$. It is found that a mesh resolution having 20 elements (Fig. 2c) has enough accuracy for the eigenvalue problem as the maximum difference of the converged leading eigenvalues for the mentioned resolution was less than 0.03% compared to a higher resolution having 25 elements (Fig. 2d) for both cases.

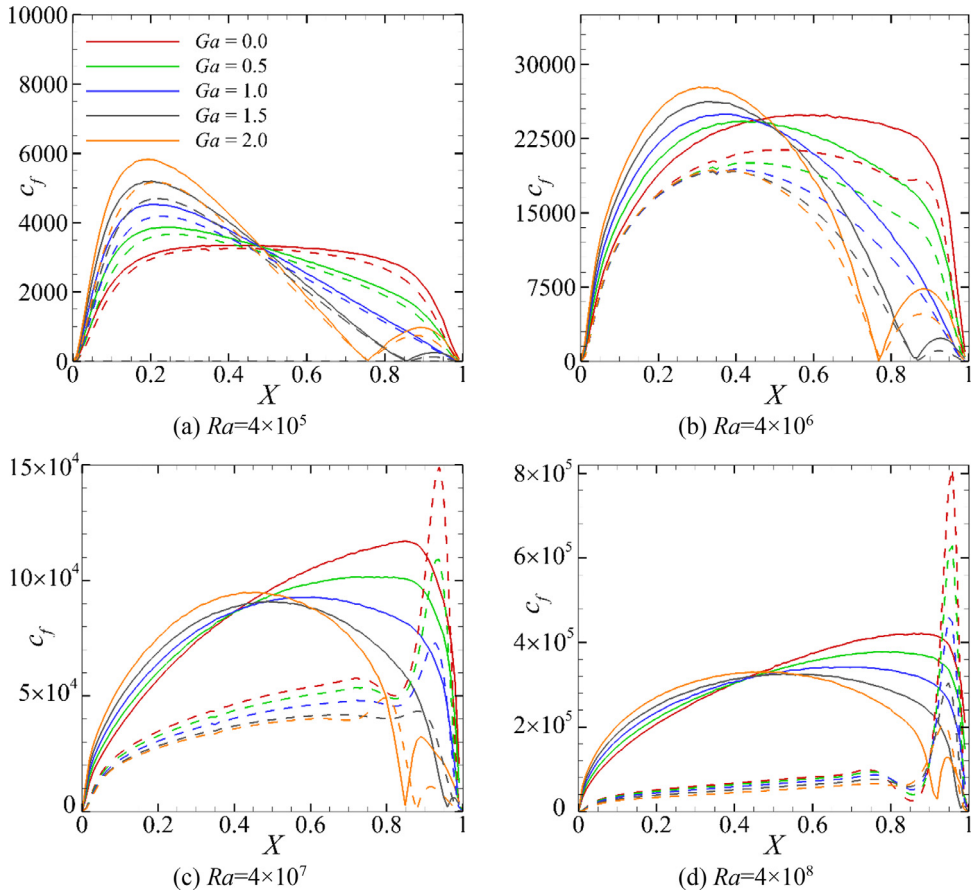

Fig. 6. Distribution of the c_f along the bottom (solid-lines) and top (dash-lines) surfaces at different Ra and Ga as stated.

5.1. Growth rates and stable regions under the Gay-Lussac type approximation

Under the GL approximation at each Ra, there exists a critical (maximum) Ga value that beyond which the flow becomes unstable. On the other hand, the Ga value is restricted to a maximum value to avoid an unphysical density ($Ga_{max} = 2$) as explained earlier in Eq. 5. Besides, the maximum Ga value is also proportional to the maximum physical Froude number at each Rayleigh and Prandtl ($Fr_{max} = Ga_{max}/RaPr$). In this respect, calculations are performed at Ga_{max} to find the primary critical Rayleigh number at which the flow becomes unstable for the first time. Thereafter, by increasing the Rayleigh number, the critical Ga value that beyond which the flow becomes unstable to 3D infinitesimal disturbances is sought. Predicted growth rates at Ga_{max} and $10^2 \leq Ra \leq 4.5 \times 10^8$ and spanwise wavenumber $0 \leq k \leq 70$ are presented in Fig. 7. The presented growth rates of disturbances in Fig. 7a and b indicate the flow remains unconditionally stable for any physical Ga value up to $Ra \leq 4 \times 10^8$. The growth rates result in Fig. 7a also indicate that the leading stable eigenvalue has a real mode for all wavenumbers up to $Ra = 10^6$. As seen, the growth rate of the leading eigenmode decreases monotonically by increasing the wavenumber in conduction dominated regime (Fig. 7a). Stability results in Fig. 7b indicate that as the Rayleigh number exceeds from 10^8, some of the leading eigenvalues turn into complex-conjugate pairs for $k \geq 32$. The growth rate results at $Ra \geq 10^8$ in Fig. 8b show a conjugate leading eigenvalue for $k \geq 16$. As seen in Fig. 7b, by increasing the Rayleigh number from 10^8 to 4×10^8, the solid lines (which connect dominant leading eigenvalues) are forming a local maximum close to the neutral stability limit ($\sigma = 0$). In Fig. 7c, the Rayleigh number is delicately increased from 4.1×10^8 to 4.5×10^8 by a small increment rate to find the primary critical Rayleigh that first produces $\sigma = 0$ and the corresponding wavenumber at which this occurs. Stability results in Fig. 7c indicate the solid-line of connecting leading eigenvalues intersects with the neutral stability line somewhere between $Ra = 4.2 \times 10^8$ and $Ra = 4.3 \times 10^8$ and $42 < k < 44$. The critical Rayleigh number at Ga_{max} is interpolated between the maximum leading eigenvalues equal to $Ra_{cr1} = 4.23 \times 10^8$ and $k_{cr1} = 43.66$. Stability results at interpolated primary critical Rayleigh number intersecting the neutral stability line ($\sigma = 0$) are checked and approved in Fig. 7d. In Fig. 7c and d ($Ra > 4 \times 10^8$), a local maximum is also observed at around $k \cong 36$, but the corresponding mode always remains in the stable region ($\sigma < 0$).

After finding the primary critical Rayleigh number, stability results are pursued at higher Rayleigh numbers. For the sake of brevity, a few stability results are presented in Fig. 8. For instance, at $Ra = 4.75 \times 10^8$ (Fig. 8a), the critical Ga value corresponding to the neutral stability occurs close to $Ga = 1.5$ while by increasing the Rayleigh number to 5×10^8 in Fig. 8b, the critical Ga value is close to 1.3. The critical Ga value intersecting $\sigma = 0$ is interpolated between two stable and unstable Ga values at each Rayleigh number. Monotonic decreasing rate of the critical Ga value by increasing the Rayleigh number with an increment rate of 0.25×10^8 continues up to $Ra = 6.25 \times 10^8$ (see Fig. 8c & d). By increasing the Rayleigh number, another local maximum is observed at around $k \cong 20$ but this mode is completely in the stable region ($\sigma < 0$). Presented stability results with $Ga = 0$ in Fig. 8e indicate the flow is unstable for $Ra \geq 6.50 \times 10^8$ with $Ga = 0$. The secondary critical Rayleigh number is interpolated equal to $Ra_{cr2} =$

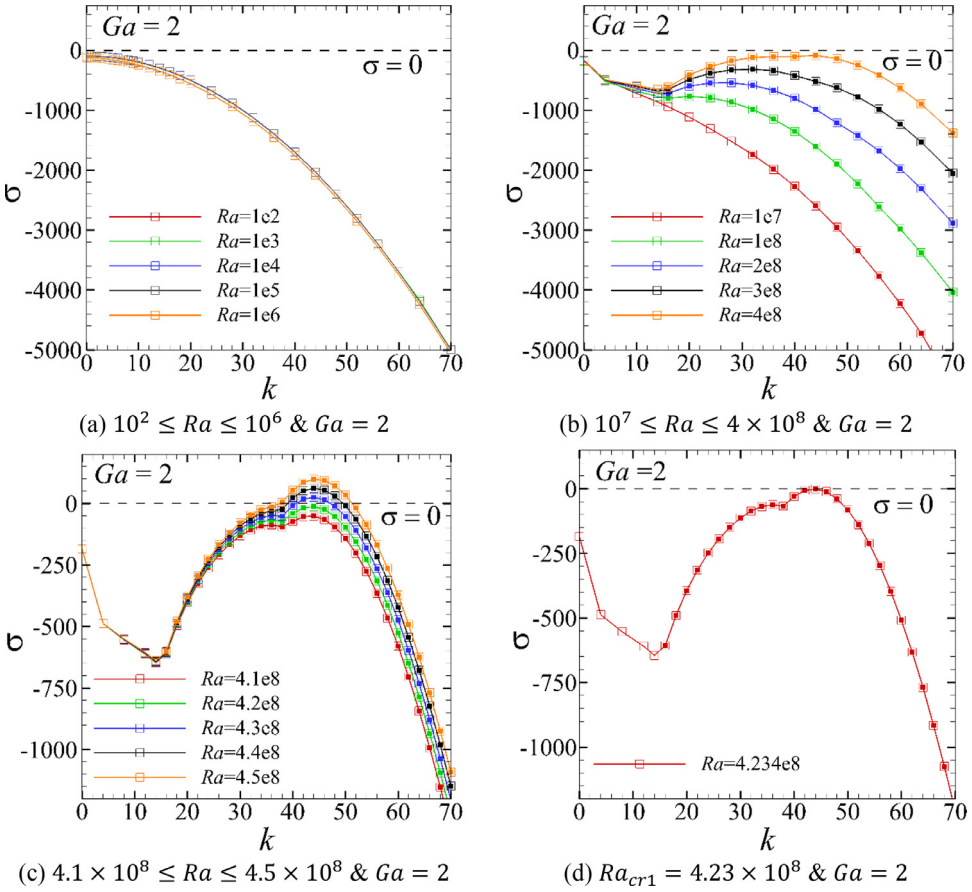

Fig. 7. Growth rates of leading eigenmodes at Ga_{max} as a function of spanwise wavenumber for (a) $10^2 \leq Ra \leq 10^6$ (b) $10^7 \leq Ra \leq 4 \times 10^8$ (c) $4.1 \times 10^8 \leq Ra \leq 4.5 \times 10^8$ (d) $Ra = 4.23 \times 10^8$. Hollow symbols represent real leading eigenvalues, while solid symbols represent complex-conjugate pairs of non-real leading eigenvalues. Solid lines connect successive dominant leading eigenvalues.

Table 2
Leading eigenmodes components at $\mathrm{Ra} = 6.5 \times 10^8$ for two different Ga values.

Ga	*Growthrate*(σ)	Angular frequency (ω)
0.15	0.462378	0.997515
0.20	0.438864	0.988598
0.25	0.417707	0.982405
0.30	0.533818	0.998714

6.46×10^8. The growth rate of the perturbations versus wavenumber at the Ra_{cr2} with $\mathrm{Ga} = 0$ is plotted in Fig. 8f, and it is found that at $\mathrm{k}_{cr} = 59.91$ it produces $\sigma = 0$.

An interesting feature is found over a small range of non-zero Ga. A small stable region at $\mathrm{Ra} = 6.50 \times 10^8$ for $0.13 \leq \mathrm{Ga} \leq 0.31$ is detected, above the critical Rayleigh number at both smaller and larger Ga. The growth rates predicted over this range are portrayed in Fig. 9a over the local $\mathrm{Ga} - \mathrm{Ra}$ parameter space. The critical wavenumber can be seen to decrease monotonically from $\mathrm{k}_{cr} = 59.1$ at $\mathrm{Ga} = 0$ down to $\mathrm{k}_{cr} \cong 54$ by $\mathrm{Ga} = 0.5$. This increasing spanwise wavelength with increasing Ga correlates with the observed widening of the sidewall structures in these flows at Ga is increased (ref. Fig. 3(c,d) and 4(c,d) in particular). This stable region vanishes by $\mathrm{Ra} = 6.51 \times 10^8$, as can be seen in Fig. 9b. This behaviour implies a complicated interplay between multiple mechanisms underlying this global stability behaviour. Nevertheless, analysis of the real and imaginary parts of the eigenmodes along the locus of maximum growth, showing only slight but monotonic variation with Ga (see Table 2) suggests that this is the result of a single instability mode, rather than an overlap between distinct modes.

Plots of the critical Rayleigh number and corresponding dominant spanwise wavenumber as functions of Ga are shown in Fig. 10. The neutral stability curve intersects with $Ga = 0$ at the secondary critical Rayleigh number, i.e. $Ra_{cr2} = 6.46 \times 10^8$. The local maximum in Ra_{cr} at $Ga \cong 0.2$ corresponds to the stabilised region identified in Fig. 9. The dominant wavenumber trend in Fig. 10b extends the observed progressive decrease with increasing Ga described previously in reference to Fig. 9; here reducing to below $k_{cr} = 44$ by $Ga = 0.2$.

Fig. 11 shows the marginal stability curves for three Ga values including $Ga = 0$, 1 and 2. The marginal curves are obtained by interpolating $\sigma(k, Ra)$ to zero growth rate for each Ra. As seen, an increase in Ga, the peak of the neutral stability curve shifts to lower wavenumbers, consistent with the aforementioned trends in Fig. 10. This reinforces that flow with a higher Ga value is less stable than a smaller Ga value.

5.2. Instability mode structure

The structure of the eigenvector fields for the neutrally stable leading instability mode at $\mathrm{Ga} = 0$, 1 and 2 will now be considered for further insight into the three-dimensional stability of these flows. It should be remembered that these fields depict the amplitude of the sinusoidal z-variation of the three-dimensional disturbance; hence these represent a slice through the perturbation at a fixed z-value. Three-dimensionality appears at the rising plume region and extends upward with the

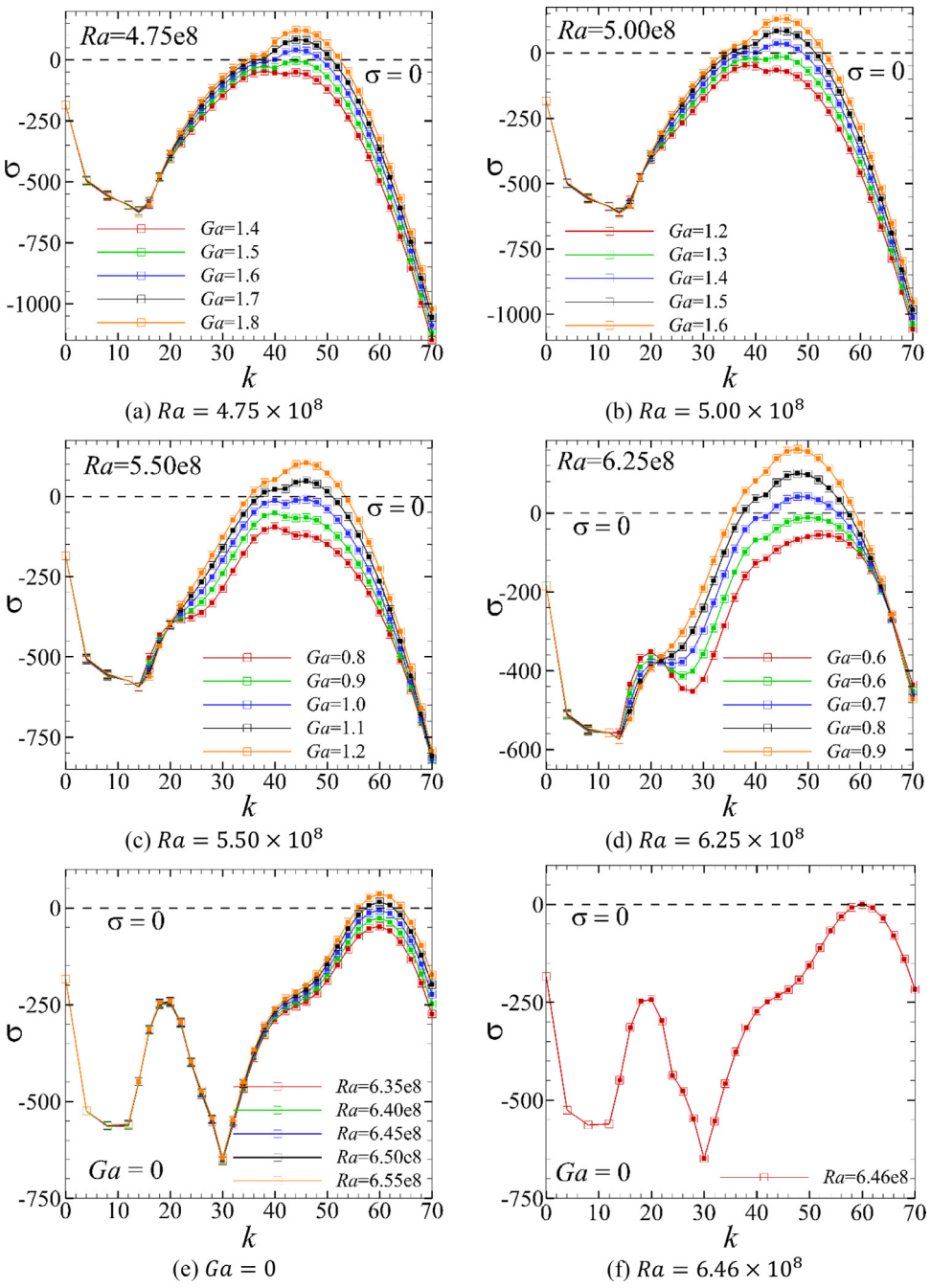

Fig. 8. Growth rates of leading eigenmodes after primary critical Rayleigh number as a function of spanwise wavenumber for (a) Ra = 4.75 $\times 10^8$ (b) Ra = 5.00 $\times 10^8$ (c) Ra = 5.50 $\times 10^8$ (d) Ra = 6.25 $\times 10^8$ (e) Ga = 0 (f) Ra = 6.46 $\times 10^8$. Hollow symbols represent real leading eigenvalues, while solid symbols represent complex-conjugate pairs of non-real leading eigenvalues. Solid lines connect successive dominant leading eigenvalues.

traversing concerning the top-right corner of the geometry as shown by the spanwise velocity component in Fig. 12. Strong spanwise velocities across the rising plume region are consistent with a mechanism involving centrifugal instability in this region. A similar counter-rotating vortices at Ga = 0 was seen in Passagia et al. [38].

5.3. Eigenvalue spectra evolution from stable to an unstable region

Thus far, only the leading eigenmode at any (Ra, Ga, k) combination has been considered. Eigenspectra containing several of the leading eigenvalues will now be considered to visualise the excursion of the leading eigenvalue as neutral stability is traversed. Fig. 13 shows the eigenvalue spectra for a representative sample case at Ra = 5 $\times 10^8$ with Ga = 1.1, 1.2, 1.3 and 1.4 and k = 44.75 (See Fig. 8b for the context on this chosen set of parameters). Stability results at this Rayleigh number and different GL parameter is already presented in Fig. 5b. The dashed-line circle in this figure indicates the onset of instability ($|\mu| = 1$). As seen, the leading eigenvalues are two complex pairs that by increasing Ga value, the first leading pair moves to the outside of the unit neutral stability circle. As seen in Fig. 13a, there are two closely grouped complex-conjugate pairs of eigenvalues, and as Ga increases the real part of the leading eigenvalue diminishes so that the faster-growing eigenmode departs rapidly from its subdominant counterpart, departing the unit circle as Ga is increased to 1.4.

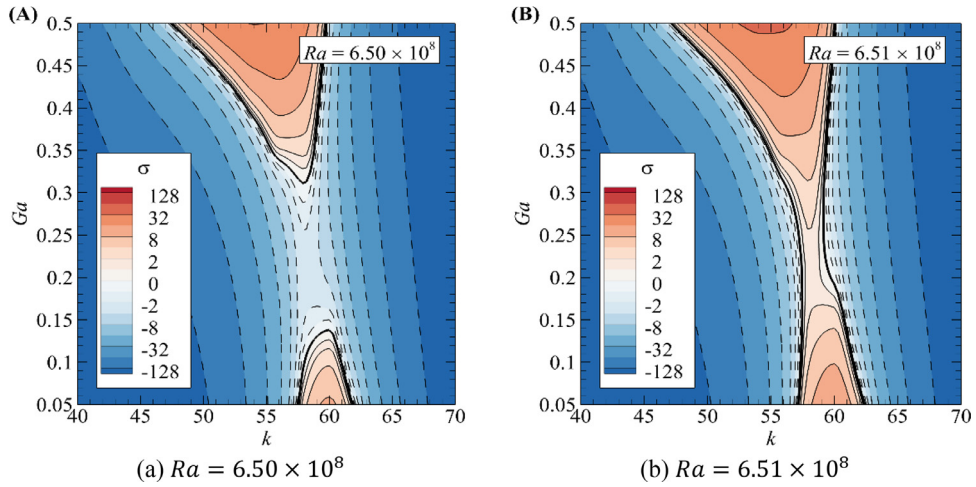

Fig. 9. Growth rate contour of the leading eigenmodes at wave number ranging $40 \leq k \leq 70$ after the secondary critical Rayleigh number as a function of GL parameter for (a) $Ra = 6.50 \times 10^8$ (b) $Ra = 6.51 \times 10^8$. The thick black line represents growth rate corresponding to neutral stability.

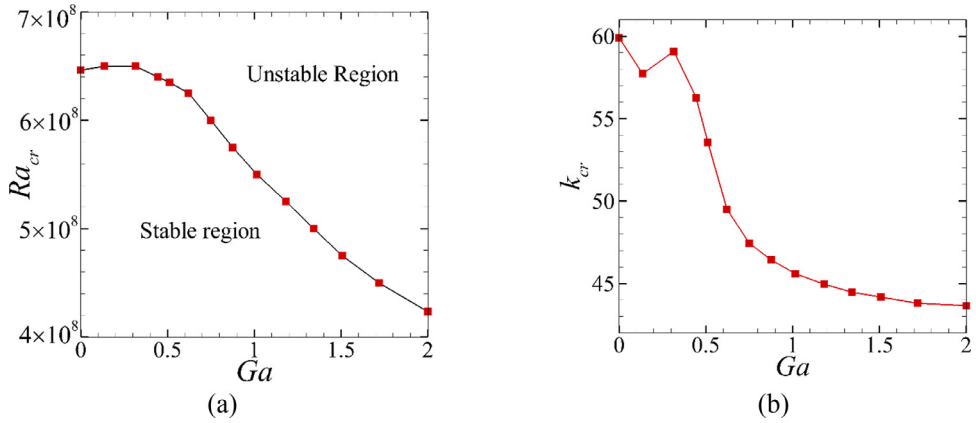

Fig. 10. Stability results for the critical (a) Rayleigh number at different Ga and (b) wavenumber at different Ga. All modes are oscillatory, in both plots.

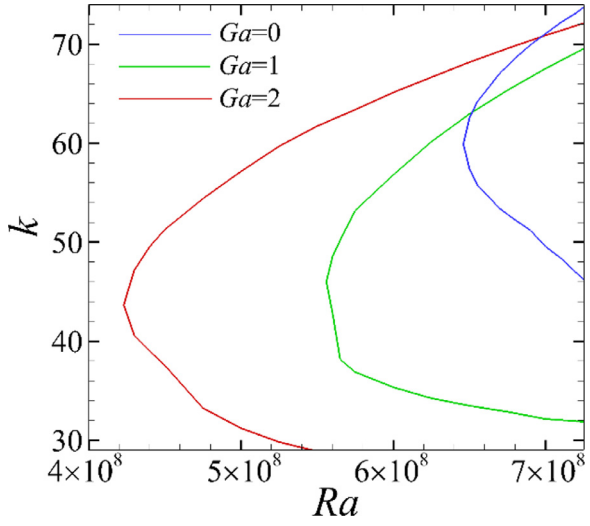

Fig. 11. Marginal stability curves for HC with Ga = 0, 1 and 2. Regions on the right of the curves represent flow conditions that are linearly unstable to 3D perturbations for that particular Ga.

The eigenvector fields corresponding to the leading eigenmode from Fig. 13(a) and (d) are visualised in Fig. 14 via plots of the spanwise vorticity, velocity and temperature perturbation fields at $Ra = 5 \times 10^8$. Fig. 14a depicts the eigenfield at Ga = 1.1, close to the onset of instability, while Fig. 15b depicts the same quantities for an unstable field (Ga = 1.4). At the lower Ga i.e. Ga = 1.1, the spanwise vorticity and velocity fields indicate that the disturbance is strongest in the region of the flow where the buoyant plume ascending along the right-hand (hot) end of the enclosure is deflected leftward by the top boundary. On the othr hand, at Ga = 1.4 the spanwise vorticity field indicates that destabilisation of the flow has advanced upstream, with disturbance vorticity structures extending the length of the right side-wall plume.

5.4. Nonlinear stability analysis to the three-dimensional state via DNS

This section presents 3D direct numerical simulation (DNS) to assess/evaluate the linear stability analysis predictions. The 3D algorithm exploits the geometry's spanwise homogeneity, combining the two-dimensional spectral-element discretisation in the x–y plane with a Fourier spectral method in the third direction normal to the x–y plane with periodic boundary conditions. Tests were conducted to determine the dependence of the computed three-dimensional solutions on the number of applied Fourier modes. In these tests, the spanwise wavenumber was selected to match a linear instability mode above the critical Rayleigh number at Ga = 0, 1, and 2. A superposition of the 2D base flow and 3D eigenvector field of the predicted linear instability was used as an initial condition. The flow was then integrated forward in time until it saturated, at which point measurements of the domain inte-

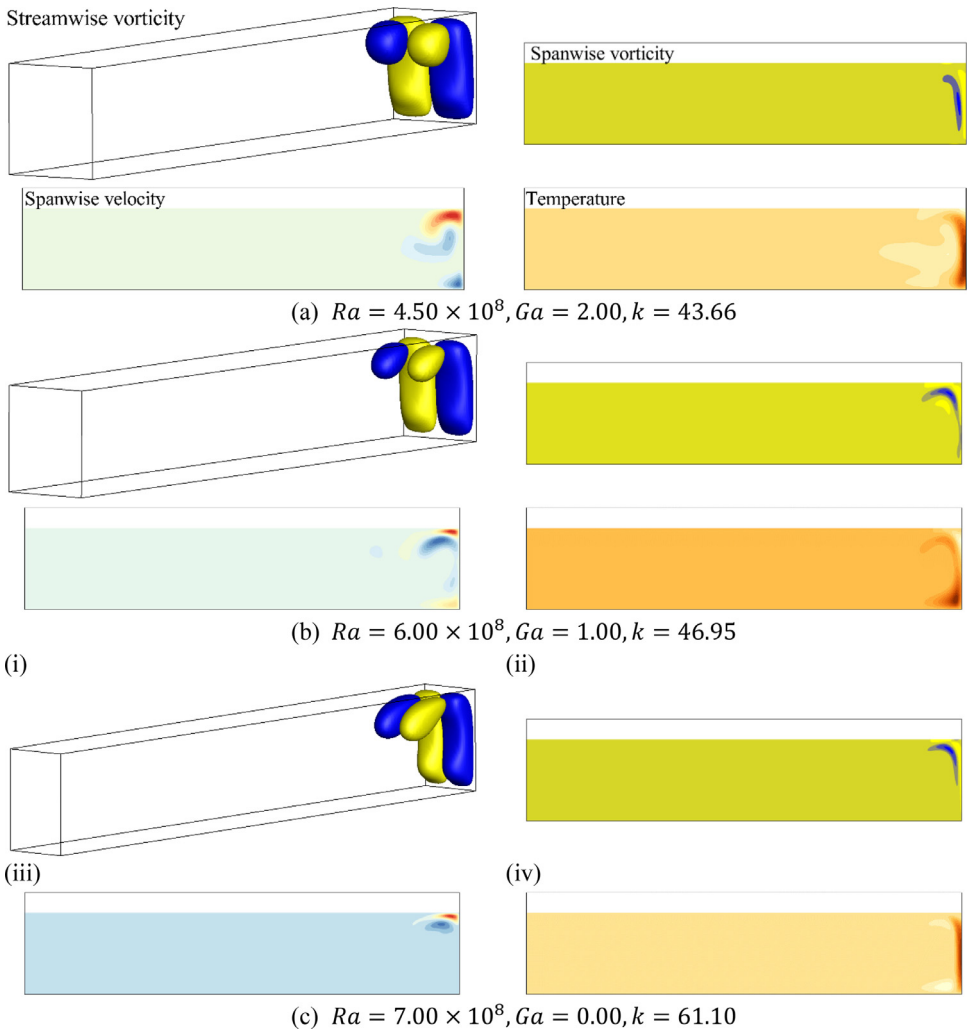

Fig. 12. (Colour online) Visualisation of the real part of leading eigenmodes at (a) Ra = 4.50 $\times 10^8$ and Ga = 2 with 43.66 (b) Ra = 6.00 $\times 10^8$ and Ga = 1 with k = 46.95 (c) Ra = 7.00 $\times 10^8$ and Ga = 0 with k = 61.10 consisting of three-dimensional visualisation of the streamwise (X-component of) vorticity, spanwise (z-component of) vorticity, spanwise velocity and temperature.

Table 3
Convergence of the saturated three-dimensional DNS solution with the number of Fourier modes included in the simulation (N_f) for a test case having Ra = 5 $\times 10^8$ and Ga = 2 with k = 45.51.

Number of Fourier modes	$\int \lvert w \rvert d\Omega$	$\lvert Difference \rvert (\%)$
2	0.188811	14.39
4	0.165055	0.20
8	0.165401	0.02
16	0.165437	–

gral of absolute velocity in the third dimension (|w|) was taken. Results of the different number of employed Fourier modes are reported in Table 3, demonstrating that the solution having 8 Fourier modes has converged to within at least four significant figures to the result obtained with 16 modes. This is supposed sufficient to capture the nonlinear growth behaviour and the mode's saturated state, so 8 Fourier modes are employed hereafter.

3D simulations were performed at Ga = 0 and 2. Rayleigh numbers are considered higher than the critical Rayleigh number corresponding to these Ga values. The spanwise wavenumbers in both cases are set to the maximum growth rate of the corresponding linear instability eigenmode. Fig. 15a and b show the time history of the spanwise velocity in three-dimensional simulations for Ra = 5 $\times 10^8$ with Ga = 2 and Ra = 7.25 $\times 10^8$ with Ga = 0, respectively. The oscillatory behaviour in Fig. 15 agrees well with the complex leading eigenmodes predicted by the linear stability analysis in Figs. 7-9. Comparing amplitude of the oscillations for the two mentioned cases indicates the flow transition to 3D periodic behaviour occurs later for a larger Ga value. In other words, flow field corresponding to a smaller Ga value faster becomes saturated to 3D periodic behaviour. In addition, comparing amplitude results indicate that the flow field with a larger Ga value has a larger amplitude of oscillations.

The growth rate of the perturbations can be calculated using the time history of energy sepctrum of the dominant Fourier mode used for w-velocity in the DNS simulation. In other words, the growth rate was obtained from the 3D DNS by finding the slope between two points in the linear growth regime from the time history of the logarithm of the kinetic energy in the first non-zero-wavenumber spanwise Fourier mode. Table 4 shows obtained growth rates via 3D-DNS and the linear stability analysis for three cases, which shows a sound agreement between two methods for three considered cases.

Fig. 16 shows 3D isosurface plots of streamwise vorticity for the cases reported in the Table 4, comparing the predicted 3D eigen-

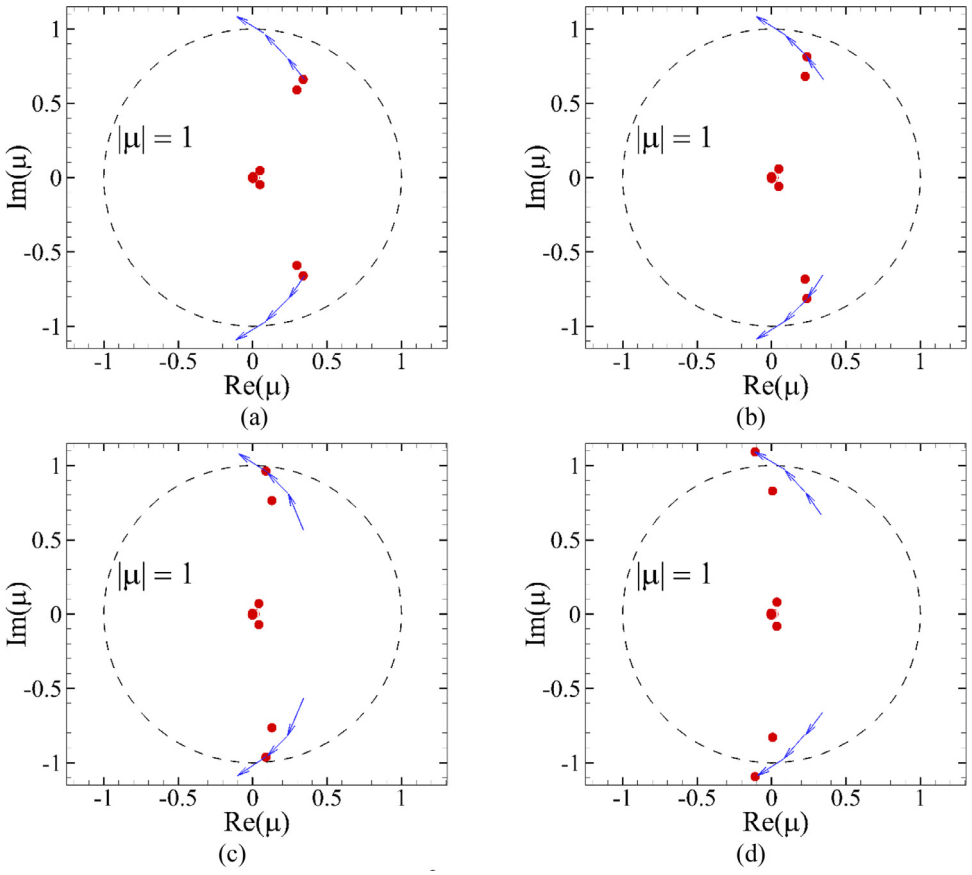

Fig. 13. Eigenvalue spectra at Ra = 5 × 10^8 with k = 44.75 and (a) Ga = 1.1, (b) 1.2, (c) 1.3, (d) 1.4. Blue arrows in each figure show the trajectory of the leading eigenmode by increasing Ga.

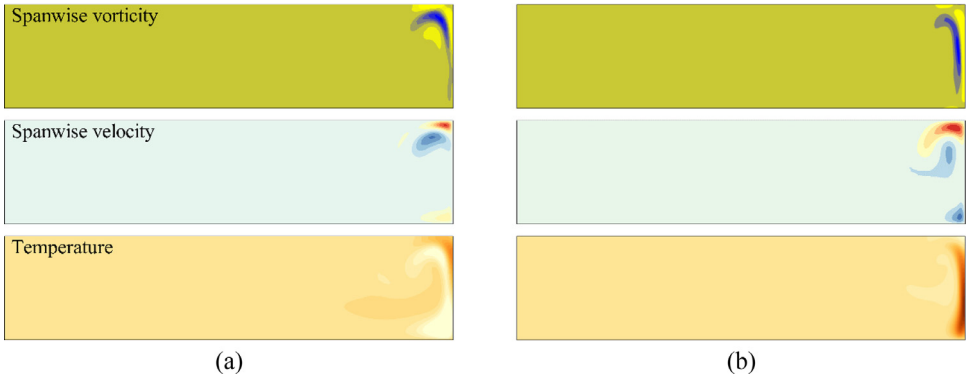

Fig. 14. Evolution of eigenvector field consisting spanwise (z-component of) vorticity and velocity and temperature at Ra = 5 × 10^8 with k = 44.75 (a) Ga = 1.1 (b) Ga = 1.4.

Table 4
Comparison between the growth rates calculated from linear stability analysis (LSA) and three-dimensional DNS.

Ga	Ra	Ra_{cr}	Ra/Ra_{cr}	k	σ(LSA)	σ(DNS)
2.00	5.00 × 10^8	4.23e8	1.18	45.51	2.72 × 10^2	2.64 × 10^2
1.01	6.50 × 10^8	5.50e8	1.18	48.25	3.15 × 10^2	3.06 × 10^2
0.00	7.25 × 10^8	6.46e8	1.12	61.63	3.23 × 10^2	3.37 × 10^2

mode in each case with the actual 3D state produced once the flow saturates following instability growth. The streamwise vorticity from the linear stability analysis (Fig. 16a-c(i)) has a good resemblance to that obtained from the three-dimensional DNS (Fig. 16a, b, c(ii)). The great agreement between the predicted eigenmode structure and the resulting saturated 3D structure verifies that the linear stability analysis provides meaningful predictions of the 3D nature of the flow. The Rayleigh numbers in Fig. 16a-c are 18% and 12% higher than the critical Rayleigh numbers for Ga = 2, 1, and 0, respectively. All three cases produce non-zero Fourier mode energy at saturation of magnitude 10^{-2} relative to the base flow energy, which is very small. The smaller the disturbance energy relative to the base flow energy, the closer the saturated state will be to the predicted infinitesimal eigenmode because the contribution of nonlinear terms is weaker that explains why a modest number (8) of Fourier modes was sufficient to resolve these 3D solutions.

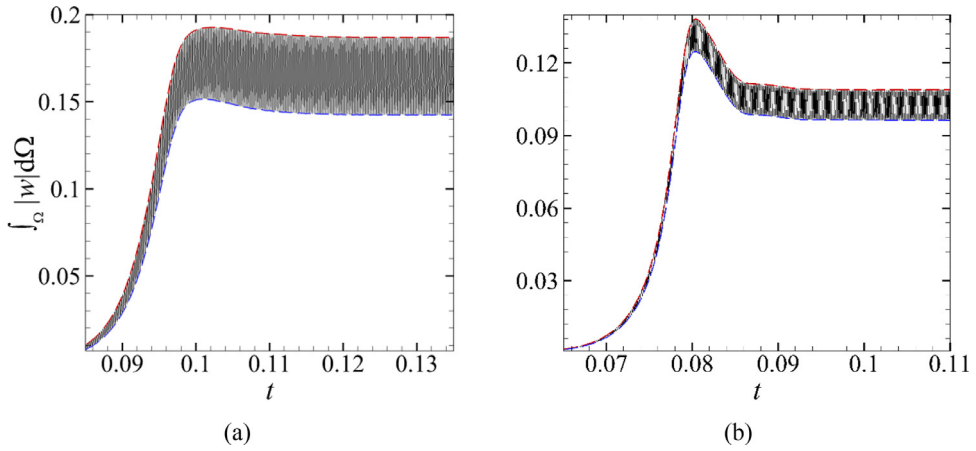

Fig. 15. Time histories of $\int |w| d\Omega$ for (a) Ga = 2 and Ra = 5.00 $\times 10^8$ with k = 45.51 and (b) Ga = 0 and Ra = 7.25 $\times 10^8$ with k = 61.63. The blue and red dashed lines demark the envelope of the oscillation of the signal.

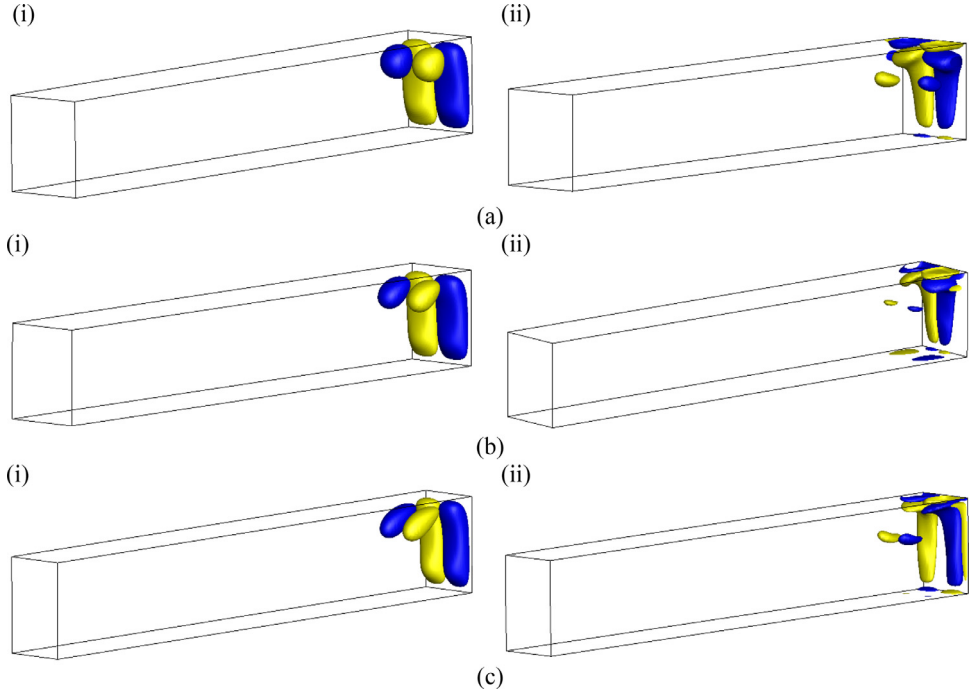

Fig. 16. Visualisation of the three-dimensional disturbances via isosurface plots of the (streamwise) x-component of vorticity for (a) Ra = 5.00 $\times 10^8$, Ga = 2, k = 45.51 (b) Ra = 6.50 $\times 10^8$, Ga = 1.01, k = 48.25 (c) Ra = 7.25 $\times 10^8$, Ga = 0, k = 61.63. In each case (i) shows the leading eigenmode predicted by the linear stability analysis and (ii) shows the saturated state of a three-dimensional DNS solution. The saturated solution in all cases is oscillatory.

6. Conclusion

Horizontal natural convection in a rectangular enclosure having an aspect ratio of height to length of 0.16 is analysed under a non-Boussinesq approximation at a Prandtl number Pr = 1. Considered non-Boussinesq approximation is a Gay-Lussac type approach under which the density variations are extended to the advection term as well as the gravity term of the momentum equation offering an improved description of rotating buoyancy-driven flows. Such a treatment inserts the Gay-Lussac parameter to the governing equations with a maximum value of 2 to avoid an unphysical density value. Many linear stability analysis were conducted to determine the critical Gay-Lussac parameters at different Rayleigh numbers that beyond which the flow becomes unstable to 3D infinitesimal disturbances. Results indicate that the flow remains unconditionally stable to any physical Gay-Lussac parameter up to the primary critical Rayleigh number which is found equal to $Ra_{cr} = 4.23 \times 10^8$. Indeed, at the primary critical Rayleigh number, the buoyancy-driven flow becomes unstable for the first time when the Gay-Lussac parameter is set to its maximum physical value. By increasing the Rayleigh number, the required Gay-Lussac parameter for an unstable buoyancy-driven flow decreases almost monotonically so that when the Gay-Lussac parameter is set to its minimum value i.e. zero, the flow field becomes unstable at the secondary critical Rayleigh number which is found equal to $Ra_{cr} = 6.46 \times 10^8$. The spanwise wavelength of the perturbations corresponding to the leading modes at the primary and secondary critical Rayleigh numbers found equal to k = 43.66 and 59.91, respectively. The stability analysis results predict that all three-dimensional transitions are via an oscillatory instability mode of the steady flow and the spanwise wavelength of the perturbations increases by increasing the Rayleigh number. Some 3D-DNS were also conducted that confirm reported stability thresholds for HC with a maximum discrepancy of 4%.

Declaration of Competing Interest

No deceleration of interest.

CRediT authorship contribution statement

Peyman Mayeli: Writing – original draft, Methodology, Conceptualization, Investigation. **Tzekih Tsai:** Writing – review & editing. **Gregory J. Sheard:** Writing – review & editing.

Acknowledgments

This research was supported by the Australian Research Council through Discovery Project DP180102647. P. M. is supported by a Monash Graduate Scholarship and a Monash International Postgraduate Research Scholarship. The authors are also supported by time allocations on the National Computational Infrastructure (NCI) peak facility and the Pawsey Supercomputing Centre through NCMAS grants. NCI is supported by the Australian Government.

References

[1] R.N. Anderson, M.A. Hobart, M.G. Langseth, Geothermal convection through oceanic crust and sediments in the Indian ocean, Science 204 (4395) (1979) 828–832.
[2] K. Brayn, M.D. Cox, A numerical investigation of the oceanic general circulation, Tellus 19 (1) (1967) 54–80.
[3] J. Yang, R. N. Edwards, J. W. Molson, Fracture-induced hydrothermal convection in the oceanic crust and the interpretation of heat-flow data, Geophys. Res. Lett., 23 (9) 929-932.
[4] S.D. King, D.L. Anderson, Edge-driven convection, Earth Planet. Sci. Lett. 160 (1998) 289–296.
[5] B.J. Foley, D. Bercovici, W. Landuyt, The conditions for plate tectonics on super-Earths: Inferences from convection models with damage, Earth Planet. Sci. Lett. 331-332 (2012) 281–290.
[6] G.O. Hughes, R.W. Griffiths, Horizontal convection, Annu. Rev. Fluid Mech 40 (2008) 185–208.
[7] H.J.J. Gramberg, P.D. Howell, J.R. Ockendon, Convection by a horizontal thermal gradient, J. Fluid Mech. 586 (2007) 41–57.
[8] S. Chiu-Webster, E.J. Hinch, J.R. Lister, Very viscous horizontal convection, J. Fluid Mech. 611 (2008) 395–426.
[9] F. Paparella, Turbulence, horizontal convection, and the Ocean's meridional overturning circulation, Math. Paradigm. Climate Sci. 15 (2016) 15–32.
[10] H.T. Rossby, On thermal convection driven by non-uniform heating from below: an experimental study, Deep Sea Res. Oceanogr. Abs. 12 (1) (1965) 9–10.
[11] G.J. Sheard, M. P.King, Horizontal convection: Effect of aspect ratio on Rayleigh number scaling and stability, Appl. Math. Model. 35 (4) (2011) 1647–1655.
[12] S. Hossain, T. Vo, G.J. Sheard, Horizontal convection in shallow enclosures scales with height, not length, at low Rayleigh numbers, Int. Comm. J. Heat Mass Transf. 109 (2018) 104308.
[13] T.K. Tsai, W.K. Hussam, A. Fouras, G.J. Sheard, The origin of instability in enclosed horizontally driven convection, Int. J. Heat Mass Transf. 94 (2016) 509–515.
[14] T.K. Tsai, W.K. Hussam, M.P. King, G.J. Sheard, Transitions and scaling in horizontal convection driven by different temperature profiles, Int. J. Therm. Sci. 148 (2020) 106166.
[15] P.Y. Passaggia, A. Scotti, B. White, Transition and turbulence in horizontal convection: linear stability analysis, J. Fluid Mech. 821 (2017) 31–58.
[16] D.V. Lyubimov, T.P. Lyubimova, N.I. Lobov, J.I.D. Alexander, Rayleigh-Benard–Marangoni convection in a weakly non-Boussinesq fluid layer with a deformable surface, Phys. Fluids 30 (2018) 024103.
[17] P. Mayeli, G.J. Sheard, Buoyancy-driven flows beyond the Boussinesq approximation: a brief review, Int. Commun. Heat Mass Transf 125 (2021) 105316.
[18] T. Pesso, S. Piva, Laminar natural convection in a square cavity: Low Prandtl numbers and large density differences, Int. J. Heat Mass Transf. 52 (3-4) (2009) 1036–1043.
[19] J.M. Lopez, F. Marques, M. Avila, The Boussinesq approximation in rapidly rotating flows, J. Fluid Mech. 737 (2013) 56–77 2013.
[20] P. Mayeli, G. Sheard, A new formulation for Boussinesq-type natural convection flows applied to the annulus cavity problem, Int. J. Numer. Methods Fluids 93 (3) (2020) 683–702.
[21] P. Mayeli, G. Sheard, Natural convection and entropy generation in square and skew cavities due to large temperature differences: a Gay-Lussac type vorticity stream-function approach, Int. J. Numer. Methods Fluids 93 (7) (2020) 2396–2420.
[22] A. Dixon, A stability analysis for interfacial waves using a Zakharov equation, J. Fluid Mech. 214 (1990) 185–210 2013.
[23] P. Mayeli, G. Sheard, An efficient and simplified Gay-Lussac approach in secondary variables form for the Non-Boussinesq simulation of free convection problems. Int. J. Numer. Method. Fluids (Published online). doi:10.1002/fld.5033.
[24] P. Mayeli, G. Sheard, A simplified and efficient Gay-Lussac approach for non-Boussinesq treatment of natural convection problems. Numer. Heat Transfer, Part B: Fundamentals (Published online). doi:10.1080/10407790.2021.1946310
[25] D. Barkley, R.D. Henderson, Three-dimensional Floquet stability analysis of the wake of a circular cylinder, J. Fluid Mech. 322 (1996) 215–242.
[26] H.M. Blackburn, J.M. Lopez, On three-dimensional quasiperiodic Floquet instabilities of two-dimensional bluff body wakes, Phys. Fluids 15 (8) (2003) L57–L60.
[27] R. Lehoucq, D. Sorensen, C. Yang, ARPACK Users' Guide, Soc. Ind. Appl. Math. (1998).
[28] G.E. Karniadakis, M. Israeli, S.A. Orszag, High-order splitting methods for the incompressible Navier–Stokes equations, J. Comput. Phys 97 (2) (1991) 414–443.